Hard X-ray ptychography at Taiwan Photon Source at 11–20 nm spatial resolution

Yi-Wei Tsai,[a]* Jhih-Min Lin,[a] Chun-Yu Chen,[a] Ying Chen,[b] Bi-Hsuan Lin,[a] Gung-Chian Yin,[a] Mau-Tsu Tang[a] and Yu-Shan Huang[a]*

[a]National Synchrotron Radiation Research Center, Hsinchu 300, Taiwan, and [b]Department of Physics, National Tsing Hua University, Hsinchu 300, Taiwan. *Correspondence e-mail: tsai.yw@nsrrc.org.tw, jade@nsrrc.org.tw

X-ray ptychography, a technique based on scanning and processing of coherent diffraction patterns, is a non-destructive imaging technique with a high spatial resolution far beyond the focused beam size. Earlier demonstrations of hard X-ray ptychography at Taiwan Photon Source (TPS) using an in-house program successfully recorded the ptychographic diffraction patterns from a gold-made Siemens star as a test sample and retrieved the finest inner features of 25 nm. Ptychography was performed at two beamlines with different focusing optics: a pair of Kirkpatrick–Baez mirrors and a pair of nested Montel mirrors, for which the beam sizes on the focal planes were 3 μm and 200 nm and the photon energies were from 5.1 keV to 9 keV. The retrieved spatial resolutions are 20 nm to 11 nm determined by the 10–90% line-cut method and half-bit threshold of Fourier shell correlation. This article describes the experimental conditions and compensation methods, including position correction, mixture state-of-probe, and probe extension methods, of the aforementioned experiments. The discussions will highlight the criteria of ptychographic experiments at TPS as well as the opportunity to characterize beamlines by measuring factors such as the drift or instability of beams or stages and the coherence of beams. Besides, probe functions, the full complex fields illuminated on samples, can be recovered simultaneously using ptychography. Theoretically, the wavefield at any arbitrary position can be estimated from one recovered probe function undergoing wave-propagating. The verification of probe-propagating has been carried out by comparing the probe functions obtained by ptychography and undergoing wave-propagating located at 0, 500 and 1000 μm relative to the focal plane.

1. Introduction

Ptychography, also known as scanning coherent diffractive imaging (SCDI), is a member of the coherent diffractive imaging (CDI) family and is a lens-less, flexible and robust method that offers high spatial resolution. The original idea of CDI was suggested by Sayre in 1980 and demonstrated by Miao *et al.* in 1999, based on the oversampling phasing method (Sayre, 1980; Miao *et al.*, 1999). The retrieving processes of a CDI technique can reveal the electron density distribution of the specimen through a single scattering pattern, which is the scattering wavefield undergoing wave-propagation from the specimen to the detector.

In ptychography, a series of scattering patterns from a light source that illuminates different regions of the specimen with partial overlaps are recorded and applied during the phase-retrieval process (Nellist *et al.*, 1995; Nellist & Rodenburg, 1998). The partially overlapped illumination of the sample during data accumulation leads to strong constraints at the time of phase retrieval, making ptychography more robust than CDI (Bunk *et al.*, 2008). Recent developments in the
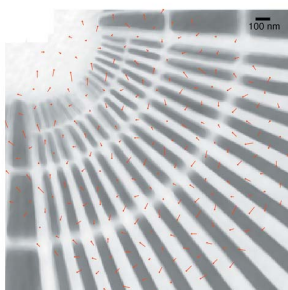
iteration algorithm using ptychography can simultaneously retrieve the image of the specimen and the beam profile of the light source (also called the probe function) (Rodenburg & Faulkner, 2004; Thibault *et al.*, 2008, 2009; Maiden & Rodenburg, 2009; Takahashi *et al.*, 2011; Thibault & Guizar-Sicairos, 2012; Pfeiffer, 2017).

The present article describes the results of hard X-ray ptychography at the Taiwan Photon Source (TPS). The demonstrations were conducted along beamlines TPS 25A1 and TPS 23A1, while phase retrieval was performed using an in-house program. This program, along with its graphical user interface (GUI), is based on MATLAB and features graphics processing unit (GPU) acceleration. An extended ptychographical iterative engine (ePIE) was adapted for the cause of methodology test.

Practically, the quality and spatial resolution of the retrieved images might suffer due to imperfections in experimental conditions, such as the partial coherence of incident beams or in the stabilities of the beams and motion stages. In order to solve this issue, the program offers compensation methods to extend the tolerance of errors arising from the above-mentioned imperfections. These compensation methods focus on non-ideal sources (partial coherent sources) (Thibault & Menzel, 2013) and beam-pointing instabilities

(Maiden *et al.*, 2012). Furthermore, the probe-extending method is proposed as a solution to the oversampling-ratio issue caused by a large beam size (Burdet *et al.*, 2014).

2. Experiments and results

Ptychography was performed at the undulator beamlines TPS 25A1 (Coherent X-ray Scattering beamline) and TPS 23A1 (X-ray Nanoprobe beamline) at TPS. The test samples for this experiment were gold-made structures patterned to a height of 650 nm on 100 nm-thick silicon nitride membranes manufactured by Applied Nanotools Inc. Siemens stars patterns with a minimum line width of 25 nm were taken as the reference points from which we determine the spatial resolutions of the images retrieved using ptychography.

A scanning electron microscope (SEM) image of the test Siemens star is shown in Fig. 1(*a*). In order to emphasize the advantage of hard X-ray ptychography, which enables the observation of thick samples because of its high penetration depth (Suzuki *et al.*, 2014; Holler *et al.*, 2014; Huang *et al.*, 2019; Takeuchi & Suzuki, 2020), we chose a pattern that was contaminated and covered for demonstration. The contamination covers the entire pattern, and the worst-case scenario is observed on the bottom-right corner of the SEM image,
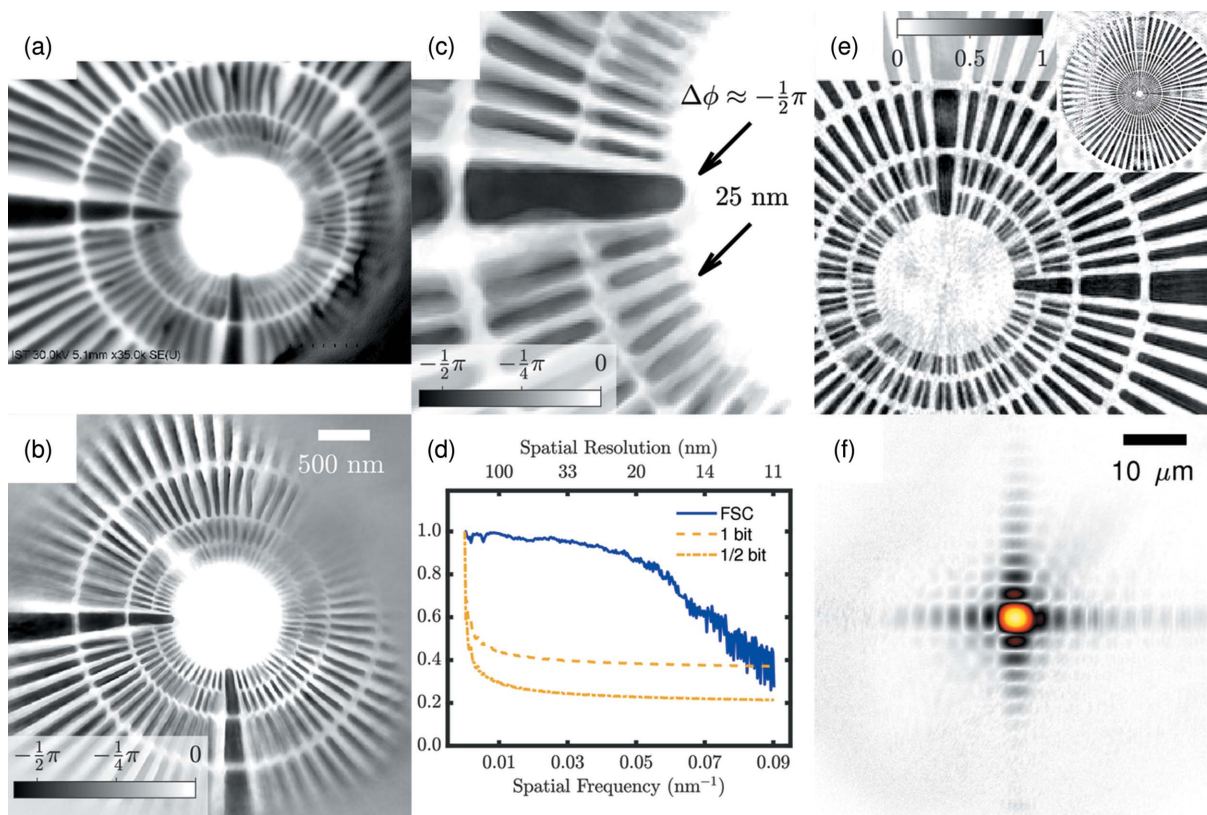

Figure 1
(*a*) SEM image of the standard sample which looks fuzzy. (*b*) Retrieved phase image of the specimen in (*a*) using ptychography at TPS 23A1. (*c*) Zoom-in version of the image in (*b*). (*d*) Fourier shell correlation (FSC) of the image in (*c*). (*e*) Ptychography result (amplitude image) at TPS 25A1. (*f*) Accompanying probe function of (*e*).

where the details of the test pattern are obscure. The retrieved phase image by ptychography with a similar field of view (FOV) in Fig. 1(a) is shown in Fig. 1(b), which is in agreement with that from the SEM. As hard X-rays are more penetrative than electron beams, the issue of contamination can be ignored in Fig. 1(b).

The measurements of Fig. 1(b) were conducted in TPS 23A1, in which the beam was focused with a pair of nested Montel mirrors (Yin *et al.*, 2016; Chen *et al.*, 2018; Lee *et al.*, 2018; Lin *et al.*, 2019, 2020). During the experiment, the photon energy was 6 keV, and beam sizes at the focal plane were approximately 100 nm × 200 nm in the horizontal and vertical directions, respectively, while the distance between the sample and detector was 1 m (the detector used here was from the Eiger 1M series, with a pixel size of 75 µm × 75 µm, manufactured by DECTRIS Ltd). The X-ray flux was approximately 10^9 photons s^{-1} at the sample position, the exposure time was 1 s at each scan position and the measurement took approximately 7 min. Figure 1(b) shows a phase image merged from three retrieved images with different but overlapped FOVs. The retrieved amount of phase shift on the structures denoted in Fig. 1(c) is approximately -0.49π, which satisfies the theoretical estimation of -0.54π when the 6 keV X-ray penetrates the 650 nm-thick Au structures. The experimental conditions of these were similar, except for the locations of the specimen relative to the focal plane; the specimen was placed at 0, 500 and 1000 µm downstream from the plane. One revealed image comprising Fig. 1(b) is shown in Fig. 1(c), where the specimen was located at the focal plane and the retrieved pixel resolution is 5.50 nm. The retrieved pixel resolutions indicate the discrete spacing in calculating and computing, not the retrieved spatial resolutions. In order to determine the retrieved spatial resolution of Fig. 1(c), independent measurements were taken from two individual retrieved images, along with the application of the Fourier shell correlation (FSC) method (Harauz & van Heel, 1986; van Heel & Schatz, 2005). The FSC of Fig. 1(c) is shown in Fig. 1(d), indicating that the spatial resolution is 11 nm. Each measurement contains 225 scattering patterns following a Fermat spiral scanning path (Huang *et al.*, 2014). The Fermat spiral in polar coordinates is defined as $r_n = c\sqrt{n}$ and $\phi_n = n\phi_0$ for the *n*th-exposure position $P_n(r, \phi)$, where *n* is the sequence index of data, *c* is a length scalar (measured to be 36.2 nm) and $\phi_0 = 137.058°$.

The results of the ptychography demonstration at TPS 25A1 focusing beams using a pair of Kirkpatrick–Baez mirrors (Lin *et al.*, 2015) are shown in Fig. 1(e), and the inset shows the same image with a wider FOV; the retrieved pixel resolution is 13.05 nm. Experimental conditions include a photon energy of 5.1 keV, beam sizes at the focal plane of approximately 3 µm along the horizontal and vertical directions, and a sample-to-detector distance of 12 m; an Eiger 16M series detector was used. The scan path was subjected to a raster scan, with an increment of 1 µm in each step. The result in Fig. 1(e) indicates not only a high spatial resolution, at which very fine features of the test pattern measuring approximately 25 nm are distinguishable, but also an extreme FOV that exceeds 25 µm.

Additionally, the spatial resolution in Fig. 1(e), determined by 10–90% line-cut method, is approximately 20 nm. Noted that the test samples used at TPS 25A1 and 23A1 are individual objects with the same specifications.

3. Beam profile reconstruction

Ptychography simultaneously yields complex density distribution functions of objects and their probe functions. For example, the probe function corresponding to the retrieved object in Fig. 1(e) is shown in Fig. 1(f). These functions are the wavefields (including amplitudes and phases) of the beam incident on the samples. Similarly, the probe function accompanying Fig. 1(b) is displayed in Fig. 2(a), where the saturation and hues indicate the amplitudes and phases, respectively. This probe function can also be drawn in terms of intensity distribution, as shown in Fig. 2(b).

The probe functions retrieved using ptychography can be applied to observe the evolution of the beam profile by changing the locations of the specimen. As mentioned, Fig. 1(b) is composed of three ptychography measurements at 0, 500 and 1000 µm downstream from the focal plane ($\Delta Z = 0$, 500 and 1000 µm); the probe functions (in terms of intensity distribution) corresponding to these results are shown in Figs. 2(b), 2(d) and 2(f), respectively. In addition, three mixture states (described in the following section) are applied to the probe during retrieving; Figs. 2(b), 2(d) and 2(f) show the first state-of-probe for each retrieval, and the proportions are 22%, 27% and 33%, respectively. The spatial resolutions of these probe functions are the same as those of the objects (of the order of 10 nm, in this case). This enables the determination of beam profiles with extreme values of spatial resolution to investigate or optimize X-ray optics.

The most impressive advantage of using ptychography to characterize beam profiles is that profiles at arbitrary positions can be estimated from a single probe function by using the
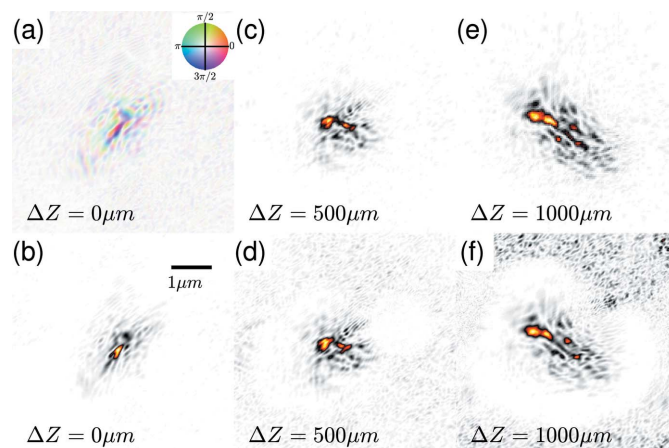

Figure 2
(a) Accompanying probe function of Fig. 1(b) with amplitudes and phases at the focal plane ($\Delta Z = 0$ µm). (b) Intensity distribution of (a). (c, e) Profiles at $\Delta Z = 500$ and 1000 µm, estimated by (a) undergoing wave-propagating. (d, f) Profiles at $\Delta Z = 500$ and 1000 µm, obtained from ptychography.
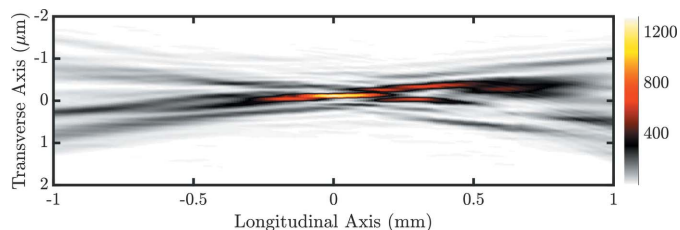
Figure 3
Beam profile along the propagating axis reconstructed by the Fresnel approximation from Fig. 2.

Fresnel approximation because they include information on all aspects of wavefields, such as amplitudes and phases. Referring to the expression for the Fresnel approximation in equation (1) (Goodman, 2005), any unknown wavefield at an arbitrary position can be obtained from a known wavefield propagated through a given distance, where $U'(x, y)$ and $U(\xi, \eta)$ are the unknown and known wavefields, respectively; x, y, ξ and η are the coordinate axes of the wavefields; k is the wavevector; and z is the distance of propagation,

$$U'(x, y) = \frac{k \exp(ikz)}{2\pi i z} \iint d\xi \, d\eta \, \left\{ U(\xi, \eta) \exp\left\{ i \frac{k}{2z} \left(\xi^2 + \eta^2\right)\right]\right\}$$
$$\times \exp\left[-i \frac{k}{z}(x\xi + y\eta)\right]. \tag{1}$$

Applying this wavefield to the focal plane shown in Fig. 2(a) enables the calculation of the reconstructed beam profiles at 500 and 1000 μm downstream; these are shown in Figs. 2(c) and 2(e), respectively. The estimated profiles are in good agreement with the measured beam shown in Figs. 2(d) and 2(f). Moreover, the entire profile of the propagating beam can be reconstructed in three dimensions with spatial resolutions of the order of 10 nm. The sliced beam profile reconstructed from Fig. 2(a) is shown in Fig. 3. Figure 3 demonstrates that ptychography is a powerful tool for optimizing the optics in

beamlines, especially for beam sizes on the nanometre scale (Giewekemeyer et al., 2013; Moxham et al., 2020).

4. Compensation methods

A ptychography retrieval program, in which ePIE was the major revealing algorithm, was constructed on MATLAB with GPU acceleration. In order to improve the quality of the retrieved images, compensating algorithms such as position correction (PC) (Maiden et al., 2012), mixture state-of-probe (MP) (Thibault & Menzel, 2013) and probe extension (PE) methods were available in the program; the effects of these methods have been characterized.

The experimental conditions for testing included photon energy, beam size and sample–detector distance of 9 keV, approximately 500 nm and 2.41 m, respectively. An image retrieved after the application of all the above compensation methods is shown in Fig. 4(a).

Position correction eliminates the effects of positioning inaccuracies due to long-term drifts of the beams and stages. The PC map is shown in Fig. 4(a), where the red points denote the 225 initially illuminated positions in the Fermat spiral and the lines indicate the shifts after the application of PC. The maximum shifts in the vertical and horizontal directions were 62 and 53 nm, respectively, while the average shift was 5.9 nm. A comparison of images obtained from FSC, with and without the PC compensation method, is shown in Fig. 4(b) (the MP method with two mix states and the PE method were enabled). PC-efficiency depends on the stability of beams and stages. In the case shown in Fig. 4, the effect of PC is not significant. But in other cases, the effect of PC compensation is prominent even for images in the same beamline.

The MP method is a powerful tool for handling irregularities in the incident beams, such as partial coherences and instabilities during exposure (Chang et al., 2018). FSCs of retrieved images (with PC and PE enabled) with different numbers of probe states are shown in Fig. 4(c). The resolution
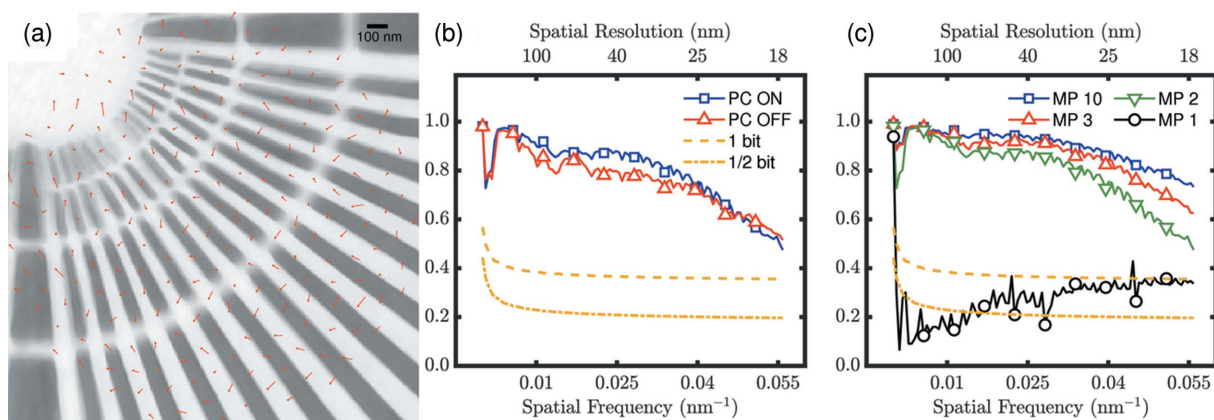

Figure 4
(a) Retrieved image with all compensation methods and position-corrected results. (b) Comparison of FSCs with and without the PC method. (c) FSC comparison of the MP method with varied mix states, where the values of MP indicate the number of mixture states applied to the probe function.

of images retrieved using a single probe function was poor, as expected, while more probe states dramatically improved the quality of the retrieved images.

4.1. Probe-extending method

In CDI and ptychography, each coherent diffraction pattern recorded by a detector corresponds to the exit wavefield immediately behind the sample. As mentioned in the previous section, the recorded pattern and exit wavefield are usually quantified simply by using Fourier and inverse Fourier transformations. The corresponding area derived from the recorded pattern, called the CDI window, can be defined as $W_{CDI} = \lambda Z/\Delta p$, where λ is the wavelength, Z is the sample-to-detector distance, and Δp is the pixel size of the detector (Edo *et al.*, 2013; Burdet *et al.*, 2014; Batey *et al.*, 2014). Denoting the beam size of the incident beam illuminating the sample as ω, the ratio S is defined as $S = W_{CDI}/\omega$, which has a significant influence on the retrieved results (Burdet *et al.*, 2014; Moxham *et al.*, 2020).

The sampling ratio S, depending on the CDI window and beam size, must be at least two in 1D cases and four in 2D cases to satisfy the Nyquist sampling. In our case, the size of the CDI window is clear, but the definition of the beam sizes is ambiguous. The beam size can usually be determined by, for example, 1σ of a Gaussian profile or the full width at half-maximum (FWHM) of the beam profile. However, interference in coherent-scattering experiments complicates the determination of beam size. For instance, the retrieved probe functions shown in Figs. 1(f) and 5(a) at TPS 25A1 and TPS 23A1 are not suitable for beam-size determination using conventional methods. In Fig. 1(f), the beam is passed through a rectangular slit, and the revealed probe function is an approximation of its diffraction pattern. Even if the main beam size is less than 2 µm, interference fringes appear, spreading over a region larger than 40 µm in diameter. In Fig. 5(a), the X-ray is focused using a pair of nested Montel mirrors. The probe function consists of a hot spot with an FWHM of approximately 200 nm, and the surrounding inter-ference fringes are spread over 4 µm. In Fig. 5(a), the intrinsic CDI window, denoted by the red frame, is 4.4 µm; therefore, the Nyquist condition is satisfied if the size of the hot spot is considered to be equal to that of the beam but not when interference fringes are considered. The FSC of the retrieved image with the intrinsic CDI window is shown by red lines denoted as PE = 1 in Fig. 5(b). Phase retrieval is unstable in this case.

The intrinsic CDI window is limited by the design parameters of beamlines. This is a serious issue in that ptychography might fail if the experimental conditions regarding the size of the beam profile are ambiguous, *i.e.* if the beam size is close to or larger than the intrinsic CDI window. When the situation arises, the information of the probe function outside the CDI window is neglected during iterations, leading to the deterioration of the retrieved resolutions. Hence, we proposed the PE method to reduce this undesired effect. The PE method simply involves applying the interpolation method to the recorded diffraction images for an equivalent reduction of the pixel sizes of the detectors. Following this, the effective CDI window is extended by the factor of interpolation. For comparison, the intrinsic and the extended CDI windows, denoted by red and black frames, respectively, are shown in Fig. 5(a). Furthermore, the FSC of the retrieved images with PE is shown in Fig. 5(b) as a blue line; significant improvements are visible. PE typically does induce artificial signals in the surroundings of the retrieved images, as shown in Fig. 5(c), but it does not influence the area covered by the scanning.

5. Conclusion

In this report, we demonstrated hard X-ray ptychography at the TPS beamlines TPS 25A1 and TPS 23A1. For test samples, spatial resolutions were approximately 20 and 11 nm at TPS 25A1 and TPS 23A1, respectively, as determined by the 10–90% line-cut and FSC methods. The retrieval is processed using a MATLAB-based in-house GUI program with GPU acceleration, which is optimized for the beamlines in TPS. The retrieval method used was ePIE, and compensation methods
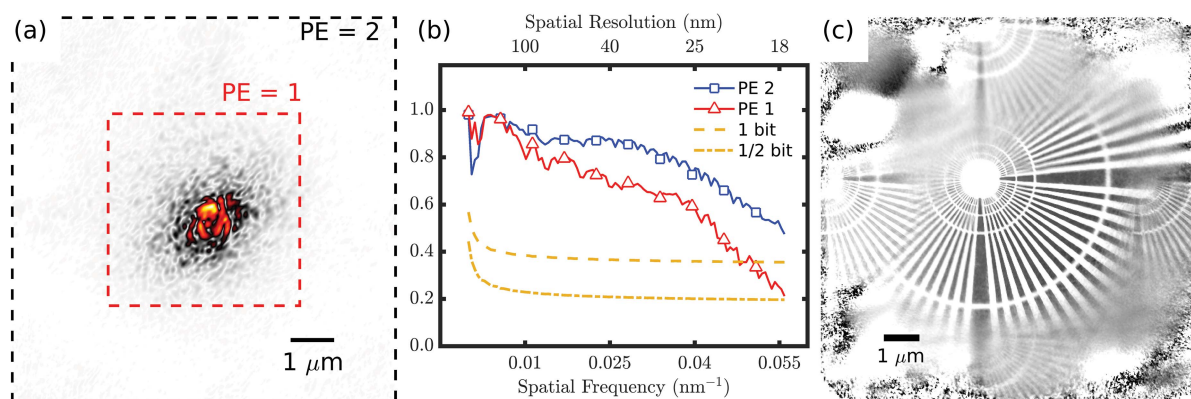

Figure 5
(*a*) Probe function accompanying Fig. 4(*a*), where the intrinsic and extended CDI windows (PE = 1 and 2, respectively) are denoted. (*b*) FSC comparison between PE = 1 and PE = 2. (*c*) Appearance of an artificial signal using PE = 2.

including the PC, MP and PE methods were used to improve the quality of the retrieved images and to increase the tolerance to error arising from experimental conditions.

References

Batey, D. J., Edo, T. B., Rau, C., Wagner, U., Pešić, Z. D., Waigh, T. A. & Rodenburg, J. M. (2014). *Phys. Rev. A*, **89**, 043812.

Bunk, O., Dierolf, M., Kynde, S., Johnson, I., Marti, O. & Pfeiffer, F. (2008). *Ultramicroscopy*, **108**, 481–487.

Burdet, N., Morrison, G. R., Huang, X., Shi, X., Clark, J. N., Zhang, F., Civita, M., Harder, R. & Robinson, I. K. (2014). *Opt. Express*, **22**, 10294–10303.

Chang, H., Enfedaque, P., Lou, Y. & Marchesini, S. (2018). *Acta Cryst.* A**74**, 157–169.

Chen, B.-Y., Yin, G.-C., Lee, C.-Y., Hsu, M.-Y., Lin, B.-H., Tseng, S.-C., Li, X.-Y., Chen, H.-Y., Wu, J.-X., Chang, S.-H. & Tang, M.-T. (2018). *Synchrotron Radiat. News*, **31**(5), 27–32.

Edo, T. B., Batey, D. J., Maiden, A. M., Rau, C., Wagner, U., Pešić, Z. D., Waigh, T. A. & Rodenburg, J. M. (2013). *Phys. Rev. A*, **87**, 053850.

Giewekemeyer, K., Wilke, R. N., Osterhoff, M., Bartels, M., Kalbfleisch, S. & Salditt, T. (2013). *J. Synchrotron Rad.* **20**, 490–497.

Goodman, J. W. (2005). *Introduction to Fourier Optics*, 3rd ed. Englewood: Roberts & Co. Publishers.

Harauz, G. & van Heel, M. (1986). *Optik*, **73**, 146–156.

Heel, M. van & Schatz, M. (2005). *J. Struct. Biol.* **151**, 250–262.

Holler, M., Diaz, A., Guizar-Sicairos, M., Karvinen, P., Färm, E., Härkönen, E., Ritala, M., Menzel, A., Raabe, J. & Bunk, O. (2014). *Sci. Rep.* **4**, 3857.

Huang, X., Yan, H., Harder, R., Hwu, Y., Robinson, I. K. & Chu, Y. S. (2014). *Opt. Express*, **22**, 12634–12644.

Huang, X., Yan, H., He, Y., Ge, M., Öztürk, H., Fang, Y.-L. L., Ha, S., Lin, M., Lu, M., Nazaretski, E., Robinson, I. K. & Chu, Y. S. (2019). *Acta Cryst.* A**75**, 336–341.

Lee, C.-Y., Yin, G.-C., Chen, B.-Y., Chen, H.-Y., Lin, B.-H., Tseng, S.-C., Chang, S.-H., Li, X.-Y. & Tang, M.-T. (2018). *Microsc. Microanal.* **24**, 104–105.

Lin, B., Li, X., Lin, D., Jian, B., Hsu, H., Chen, H., Tseng, S., Lee, C., Chen, B., Yin, G., Hsu, M., Chang, S., Tang, M. & Hsieh, W. (2019). *Sci. Rep.* **9**, 207.

Lin, B.-H., Wu, Y.-H., Li, X.-Y., Hsu, H.-C., Chiu, Y.-C., Lee, C.-Y., Chen, B.-Y., Yin, G.-C., Tseng, S.-C., Chang, S.-H., Tang, M.-T. & Hsieh, W.-F. (2020). *J. Synchrotron Rad.* **27**, 217–221.

Lin, J.-M., Chen, C.-Y. & Huang, Y.-S. (2015). *Construction Design Report of TPS 25A1*, http://tpsbl.nsrrc.org.tw/userdata/upload/25A/DDR%20TPS%2025A.pdf.

Maiden, A., Humphry, M., Sarahan, M., Kraus, B. & Rodenburg, J. (2012). *Ultramicroscopy*, **120**, 64–72.

Maiden, A. M. & Rodenburg, J. M. (2009). *Ultramicroscopy*, **109**, 1256–1262.

Miao, J., Charalambous, P., Kirz, J. & Sayre, D. (1999). *Nature*, **400**, 342–344.

Moxham, T. E. J., Parsons, A., Zhou, T., Alianelli, L., Wang, H., Laundy, D., Dhamgaye, V., Fox, O. J. L., Sawhney, K. & Korsunsky, A. M. (2020). *J. Synchrotron Rad.* **27**, 1688–1695.

Nellist, P. D., McCallum, B. C. & Rodenburg, J. M. (1995). *Nature*, **374**, 630–632.

Nellist, P. D. & Rodenburg, J. M. (1998). *Acta Cryst.* A**54**, 49–60.

Pfeiffer, F. (2017). *Nat. Photon.* **12**, 9–17.

Rodenburg, J. M. & Faulkner, H. M. L. (2004). *Appl. Phys. Lett.* **85**, 4795–4797.

Sayre, D. (1980). *Imaging Processes and Coherence in Physics*, pp. 229–235. Berlin, Heidelberg: Springer.

Suzuki, A., Furutaku, S., Shimomura, K., Yamauchi, K., Kohmura, Y., Ishikawa, T. & Takahashi, Y. (2014). *Phys. Rev. Lett.* **112**, 053903.

Takahashi, Y., Suzuki, A., Zettsu, N., Kohmura, Y., Senba, Y., Ohashi, H., Yamauchi, K. & Ishikawa, T. (2011). *Phys. Rev. B*, **83**, 214109.

Takeuchi, A. & Suzuki, Y. (2020). *Microscopy*, **69**, 259–279.

Thibault, P., Dierolf, M., Bunk, O., Menzel, A. & Pfeiffer, F. (2009). *Ultramicroscopy*, **109**, 338–343.

Thibault, P., Dierolf, M., Menzel, A., Bunk, O., David, C. & Pfeiffer, F. (2008). *Science*, **321**, 379–382.

Thibault, P. & Guizar-Sicairos, M. (2012). *New J. Phys.* **14**, 063004.

Thibault, P. & Menzel, A. (2013). *Nature*, **494**, 68–71.

Yin, G.-C., Chang, S.-H., Chen, B.-Y., Chen, H.-Y., Lin, B.-H., Tseng, S.-C., Lee, C.-Y., Wu, J.-X., Wu, S.-Y. & Tang, M.-T. (2016). *AIP Conf. Proc.* **1741**, 030004.